



3D printed polylactic acid (PLA) filters reinforced with polysaccharide nanofibers for metal ions capture and microplastics separation from water

Natalia Fijoł^{a,b}, Andrea Aguilar-Sánchez^a, Maria-Ximena Ruiz-Caldas^a, Jakob Redlinger-Pohn^c, Andreas Mautner^d, Aji P. Mathew^{a,b,*}

^a Department of Materials and Environmental Chemistry, Stockholm University, Frescativägen 8, 106 91, Stockholm, Sweden

^b Wallenberg Wood Science Center, Teknikringen 56-58, 100 44, Stockholm, Sweden

^c Department of Fibre and Polymer Technology, KTH Royal Institute of Technology, Teknikringen 56–58, 114 28 Stockholm, Sweden

^d Polymer and Composite Engineering (PaCE) Group, Institute of Materials Chemistry and Research, Faculty of Chemistry, University of Vienna, Währinger Str. 42, 1090 Wien, Austria

ARTICLE INFO

Keywords:

Metal ion removal
Microplastics removal
3D printing
Polylactic acid
Nanocellulose
Nanochitin

ABSTRACT

The need for multifunctional, robust, reusable, and high-flux filters is a constant challenge for sustainable water treatment. In this work, fully biobased and biodegradable water purification filters were developed and processed by the means of three-dimensional (3D) printing, more specifically by fused deposition modelling (FDM).

The polylactic acid (PLA) – based composites reinforced with homogenously dispersed TEMPO-oxidized cellulose nanofibers (TCNF) or chitin nanofibers (ChNF) were prepared within a four-step process; *i.* melt blending, *ii.* thermally induced phase separation (TIPS) pelletization method, *iii.* freeze drying and *iv.* single-screw extrusion to 3D printing filaments. The monolithic, biocomposite filters were 3D printed in cylindrical as well as hourglass geometries with varying, multiscale pore architectures. The filters were designed to control the contact time between filter's active surfaces and contaminants, tailoring their permeance.

All printed filters exhibited high print quality and high water throughput as well as enhanced mechanical properties, compared to pristine PLA filters. The improved toughness values of the biocomposite filters clearly indicate the reinforcing effect of the homogenously dispersed nanofibers (NFs). The homogenous dispersion is attributed to the TIPS method. The NFs effect is also reflected in the adsorption capacity of the filters towards copper ions, which was shown to be as high as 234 and 208 mg/g_{NF} for TCNF and ChNF reinforced filters, respectively, compared to just 4 mg/g for the pure PLA filters. Moreover, the biocomposite-based filters showed higher potential for removal of microplastics from laundry effluent water when compared to pure PLA filters with maximum separation efficiency of 54 % and 35 % for TCNF/PLA and ChNF/PLA filters, respectively compared to 26 % for pure PLA filters, all that while maintaining their high permeance.

The combination of environmentally friendly materials with a cost and time-effective technology such as FDM allows the development of customized water filtration systems, which can be easily adapted in the areas most affected by the inaccessibility of clean water.

1. Introduction

The contamination of the water sources by various pollutants such as heavy metals [1] and petroleum-based microplastics [2], which are defined as ‘any solid plastic particles insoluble in water with dimensions between 1 μm and 1 mm’ [3] is a developing issue threatening natural environment and human health. Effluents from vast industrial plants are one of the main sources of chemical pollution. Copper, as the second most abundantly used non-ferrous metal in the metallurgic industry [4],

ends up together with many other metals and metalloids in the landfills in the form of billions of tones of slags, dust, and aerosol by-products as waste from metal ore mining industry [5]. This can further lead to water contamination and in consequence negatively impact both wildlife [6] and human health [7]. As it comes to microplastics, their release into water stems from effluents of wastewater treatment plants, textile and fishing industries [8]. Moreover, microplastic accumulation in the environment is escalated by the utilization of household washing machines. In a recent study Galvão et al. [9] showed that a 6 kg load of

* Corresponding author at: Department of Materials and Environmental Chemistry, Stockholm University, Frescativägen 8, 106 91, Stockholm, Sweden.

E-mail address: aji.mathew@mmk.su.se (A.P. Mathew).

<https://doi.org/10.1016/j.cej.2022.141153>

Received 14 December 2022; Received in revised form 21 December 2022; Accepted 22 December 2022

Available online 24 December 2022

1385-8947/© 2022 The Authors. Published by Elsevier B.V. This is an open access article under the CC BY-NC license (<http://creativecommons.org/licenses/by-nc/4.0/>).

laundry emits 18,000,000 synthetic microfibers into the environment, out of which the majority is in the size range between 50 and 100 μm . It is therefore crucial to develop filtrating methods fitting the commercial household washing machines to minimize the impact of household laundry on the environment. It is important to address the problem of water contamination by using sustainable solutions, which are in line with the principles of circular economy [10]. That is why the utilization of biobased composites for the development of green filtration systems is gaining scientific interest.

Poly(lactic acid) (PLA) is an aliphatic polyester built out of lactic acid monomers, which can be obtained from renewable resources e.g. sugarcane and corn [11]. PLA is often used as a matrix phase for the preparation of biocomposites due to its renewability, biodegradability, and ease of processing [11]. The chosen dispersed phase for such composites often include cellulose and/or chitin. These are fully biobased materials that can be extracted from plants, bacteria and tunicates in the case of cellulose [12] and e.g. exoskeleton of crustaceans, mushrooms, nematodes, and insects in the case of chitin [13]. They are often processed into nanofibers (NFs) via various mechanical isolation processes including e.g. high-pressure homogenization [14] and cryocrushing [15]. The dispersion of non-modified, hydrophilic biopolymer NFs in nonpolar PLA matrix results in immiscible composite blends of low interfacial compatibility, low resistance, and water barrier properties as well as poor matrix-dispersed phase interactions [16,17]. Moreover, the agglomerated NFs lead to impaired mechanical properties of final composite products [18]. Previous studies report the development of PLA-based composites reinforced with cellulose and chitin NFs via solution casting [19], direct melt compounding by extrusion [20], compression moulding [21] as well as via melt spinning [22]. The challenge of a homogenous dispersion of cellulose and chitin NFs in the PLA matrix is addressed by the addition of e.g. silane coupling agent [19], polyethylene glycol [22], activated biochar [20] and chitosan [21]. Additionally, NFs can be subjected to chemical and/or surface modifications such as grafting [23], esterification [24] or acetylation [25,26] to achieve better interphase compatibility between the fibers and the composite matrix.

Thermally induced phase separation (TIPS) method can be another plausible way to enhance the NFs dispersion in the PLA matrix. TIPS relies on bringing a multicomponent system, such as a composite blend constituting out of polymer matrix and dispersed phase, into a thermodynamically unstable state inducing the separation of the system into two distinct phases i.e. polymer-rich and polymer-lean phase. The solvent is then removed by e.g. freeze drying which leads to the development of highly porous matrices [27,28]. The process was previously shown to improve the dispersion of nanomaterials in PLA matrix leading to improved mechanical properties of composite films [29,30] and scaffolds [29,31]. The development of functional composites for biomedical [31–33] and water treatment [34] applications by combining TIPS method with three-dimensional (3D) printing technology was previously reported.

3D printing also called additive manufacturing (AM) yields the desired shape by applying one layer of material at a time based on a computer-aided design (CAD) model [35]. Fused Deposition Modelling (FDM) is one of the methods of 3D printing, which relies on the introduction of a thermoplastic filament into a heated chamber and the deposition of the melted material onto the print bed. FDM is a cost- and energy- efficient method, which does not require expensive tools and avoids post-processing [35,36]. Therefore, FDM offers the possibility to produce customized, highly functional water purification filters with tuned porous structures. Moreover, as 3D printing becomes more and more available worldwide, it allows producing portable water purification filters at the point and time of need. Several studies have reported the use of 3D printing for the development of water purification systems [37–39]. However, there are only a few works that combine all three concepts i.e. 3D printing, green polymer-based materials and water treatment applications [40]. There are reports on 3D-printed water

treatment systems based on green polymers such as PLA [34,41,42], alginate [43,44], cellulose acetate [45,46] and chitosan [47–49].

This study aims to reinforce easily 3D-printable PLA bioplastic with TEMPO-oxidized cellulose nanofibers (TCNF) and chitin nanofibers (ChNF), which are characterized by high surface area and charge [50,51], to develop highly functional, 3D water purification filters manufactured using scalable and inexpensive FDM process. Different geometries and porous architectures of the filters were designed to investigate their influence on the final permeance and adsorption behaviour of the filters. The performance of the filters for water treatment applications in laboratory conditions was investigated, reporting the removal of copper ions by adsorption and the removal of microplastics by both physical interactions and size exclusion. We hypothesize that the studied approach provides an opportunity to utilize the surface chemistry of the biocomposite material for the adsorption of molecular pollutants, while also exploiting the tailored pore architecture of the filters for the separation of bigger suspended particles e.g. microplastics by size exclusion.

Thus, this study provides a low-cost, custom-optimized, and environmentally friendly route to prepare monolithic and mechanically enhanced PLA-based composite filters with high permeance performance suitable for further functionalization. The developed filters are potentially applicable for the removal of a variety of water contaminants ranging from small to big molecules.

2. Experimental

2.1. Materials and methods

The raw materials used for the preparation of 3D printable biocomposites were: transparent extrusion grade PLA pellets (Ingeo™ Biopolymer 4043D, Nature Works, provided by Add North 3D AB, Sweden), 1,4-dioxane (anhydrous, 99.8 %, Carlo Erba Reagents, Spain), the 1.5 wt% water suspension of TEMPO (2,2,6,6-tetramethylpiperidine-1-oxyl radical)-mediated oxidized cellulose nanofibers (TCNF, 1.1 mmol/g of carboxyl groups) provided by Swiss Federal Laboratories for Materials Science and Technology (EMPA), Switzerland. The dimensions of nanofibers, as studied by atomic force microscopy (AFM), were in the range of 3–5 nm and lengths in μm scale [52] (Figure S1). Chitin nanofibers (ChNF, 2 wt% in water suspension, with less than 5 wt% of deacetylation degree) with a specific surface area of 200 m^2/g and polymerization degree of 300 were provided by BiNF-i, Sugino Machine Limited, Japan. AFM study of ChNF showed fibrils diameter of 3 nm and lengths in nm- μm scale (Figure S1). The commercial 3D printing filament used for printing out reference models was a transparent PLA filament (Add North, 3D AB, Ölsremma, Sweden). The reagent used for the metal adsorption study was copper (II) sulfate pentahydrate (99 %, Acros Organics, Belgium).

The laundry water sample containing microplastics was donated by Mimby AB (Gothenburg, Sweden).

Preparation of TCNF/ChNF/PLA composites: The master batch of the composite solution was prepared using a modification of the protocol reported in our previous work on hydroxyapatite/PLA biocomposite system [34]. In brief, a 10 % PLA/1,4-dioxane solution was prepared by dissolving the transparent, commercial PLA pellets in 1,4-dioxane solution and overnight magnetic stirring at room temperature. Then, a measured amount of either TCNF (1.5 wt% suspension) or ChNF (2 wt% suspension) was added to the solution and magnetically stirred for 2 h leading to 5 wt% nanofiber (NF)/PLA suspension. The obtained TCNF/PLA or ChNF/PLA suspensions were then added drop-wise into the liquid nitrogen forming NF/PLA biocomposite pellets. The pellets were further freeze-dried for 48 h. The final, freeze-dried product was single-screw extruded at a feed temperature of 180 °C and screw speed of 100 rpm into 3D printing filaments with a dimension of 2.85 mm.

3D printing: The shapes of the filters were based on cylindrical and hourglass-shaped CAD models. The dimensions, as well as the porous

structure, were designed with the use of CURA slicing software prior generating the G-code file necessary for being processed by the printer. The printer used was an Ultimaker S5 (Ultimaker BV, The Netherlands). The general printing parameters used for both the biocomposite and reference commercial PLA filaments were: nozzle diameter 400 μm , bed temperature 60 $^{\circ}\text{C}$, printing speed 35–55 mm/s, layer thickness 150 μm , shell thickness 500 μm . The nozzle temperature was set to 200 $^{\circ}\text{C}$ and 220 $^{\circ}\text{C}$ for the PLA and biocomposite systems, respectively.

Printing parameters for the filters: Four different models were printed and tested for each composite system and reference PLA. These included (i) uniform porosity and (ii) three-level gradient porosity cylindrical filters, as well as the (iii) uniform porosity and (iv) two-level gradient porosity hourglass-shaped filters. The printing dimensions of the samples were varied depending on the experiment of choice (i.e. 40 \times 40 \times 40 mm, 20 \times 20 \times 20 mm and 10 \times 10 \times 10 mm), however the porous structure (size, geometry) and proportions were kept consistent.

The printing parameters for cylindrical filters were: infill density: 10 %, infill line distance: 1.5 mm, infill pattern: grid, wall thickness: 0.5 mm, printing speed: 45 mm/s.

The printing parameters for hourglass shapes filters were: infill density: 10 %, infill line distance: 1.5 mm, infill pattern: lines, wall thickness: 0.2 mm, printing speed: 55 mm/s.

2.2. Characterization of the biocomposite system

Scanning Electron Microscopy (SEM): The morphology of the biocomposite pellets and 3D printing filaments as well as the pore structure of the 3D printed porous filters, was investigated with the use of a Hitachi TM3000, Tabletop Microscope (Hitachi Ltd, Japan) and a JEOL JSM-7000F Analytical Scanning Electron Microscope (JEOL Ltd, Japan). The samples were analysed at an accelerating voltage of 5 kV and 15 kV in both secondary electron and back-scattered electron modes. All the samples were prepared for the microscope examination by sputtering with a thin layer of gold (for 60 s, at 10 mA and from a 30 mm distance). The pore size of each model was measured based on each porosity level cross-section from the obtained SEM image using *ImageJ* software.

Thermogravimetric Analysis (TGA): The thermal decomposition of the composites in the form of freeze-dried pellets and custom extruded biocomposite filaments as well as their corresponding PLA references were analysed with the use of a Discovery TGA (TA Instruments Inc., United States). The samples were weighted to fractions of between 15 and 25 mg, placed in high-temperature platinum holders, and then heated from 30 $^{\circ}\text{C}$ up to 550 $^{\circ}\text{C}$ at a heating rate of 10 $^{\circ}\text{C}/\text{min}$ under airflow of 20 mL/min. The following data were obtained based on the thermograms: T_{onset} (temperature at which the degradation starts), $T_{50\%}$ (temperature at which loss of 50 wt% of the material occurs), and T_{endset} (temperature at which less than 99 wt% material is degraded).

X-ray Diffraction (XRD): The crystallinity of the TCNF/PLA and ChNF/PLA 3D printing filaments and starting materials (i.e. PLA pellets and TCNF and ChNF films prepared from the starting gels) was assessed by XRD. All of the tested samples were in the form of casted films. The instrument used was a PANalytical X'Pert PRO MRD City (Malvern Instruments, UK) with copper radiation ($\lambda = 1.54056 \text{ \AA}$) and a scan range between $2\theta = 5^{\circ}$ and 40° .

Fourier-transform Infrared Spectroscopy (FTIR): The PLA pellets, filaments, and 3D printed parts as well as their corresponding synthesized TCNF/PLA and ChNF/PLA biocomposite pellets, filaments, and 3D printed parts were analysed by infrared spectroscopy with a Varian 610-5 IR FT-IR spectrometer (Varian Inc., CA, USA) equipped with the Specac Golden Gate single reflection attenuated total reflection (ATR) accessory with a diamond ATR element (Specac, UK). Sixteen scans between 4000 cm^{-1} and 400 cm^{-1} were averaged for each spectrum at intervals of 1 cm^{-1} with a resolution of 4 cm^{-1} . Each sample was measured three times.

The characterization of biocomposite systems is discussed in

Supplementary Information. The compiled TGA, XRD and FT-IR results are presented in [Figure S2](#).

2.3. Characterization of the 3D printed composites

Mechanical testing: Compressive tests of the printed models were performed with following the Standard Test Method D695-15 on specimens in the cuboid shape with dimensions of 12.7 \times 12.7 \times 25.4 mm and a print infill density of 40 %. 30 samples were tested in total (10 for each composite system and reference PLA system, out of which 5 were uniformly porous and 5 had gradient porous structure). Specimens were conditioned before analysis for 48 h in a conditioning chamber at 23 $^{\circ}\text{C}$ and 51 % relative humidity. A 10 kN load cell and a compression rate of 1 mm/min until 60 % deformation was reached were applied. Tests were performed by applying the force perpendicular to the printing direction on an Instron 5960 dual column universal test frame (Instron Corporation, USA) in a controlled environment (23 $^{\circ}\text{C}$ and 51 % relative humidity). The apparent compressive elastic modulus was calculated from the slope of the linear elastic section of the stress-strain curves, without considering the plateau and the densification regime. The energy dissipation, i.e. toughness of the samples, was calculated considering the area under the stress-strain curve.

Permeance measurements: The water permeance of the bio-based filters was measured using an in-house constructed water permeance instrument in dead-end filtration mode ([Figure S3](#)). The measurements were conducted at room temperature and a water temperature of 20 $^{\circ}\text{C}$ at a constant flow-rate of 1500 cm^3/min . The permeance of the samples was assessed by measuring the exact time (t) needed for 2 L of water (V) to pass through the filter with a cross-sectional area (A) (Eq. (1)). The pressure difference between filter's inlet and outlet was measured. There were five experimental repetitions for each filter design and material.

$$\text{Permeance} = \frac{V}{t \times A \times p} \quad (1)$$

Batch adsorption tests: The metal ion adsorption capability of filters was assessed by immersing the 3D printed hourglass-shaped filters with uniformly porous structure (weighing between 1.5 and 2.5 g dependent on the 3D printing filament used) in 80 mL of 1 mM or 10 mM aqueous solutions of copper sulfate. The adsorption tests were conducted at a pH range between 6.0 and 7.5. These pH values were chosen based on the previous literature reports, which have reported optimal adsorption of copper ions in these conditions [53,54] and based on the conducted surface zeta potential measurements confirming the negatively charged surface of the 3D printed filters at that pH range ([Figure S3](#)). The adsorption experiments were carried out at room temperature under magnetic stirring (450 rpm). The filtrate samples with a volume of approximately 15 mL were collected after 30 min, 1 h, 3 h, 6 h, and 8 h. The metal concentration in the collected aliquots was assessed with the UV-vis spectrophotometer (GenesysTM, 40/50, ThermoFisher) using the colorimetric method ($\lambda^{\text{max}} = 810 \text{ nm}$). The adsorbed copper ions were desorbed from the filters with a hydrochloric acid treatment (immersion of the filters in 80 mL of 10 M HCl), followed by immersion in deionized water at room temperature and overnight air-drying. Adsorption-desorption experiments were repeated three times on the set of three filters for each material to assess the recyclability of the developed filters. The adsorption capacity (q_e , mg/g) and adsorption efficiency (%) were calculated with Equations (2) and (3), respectively.

$$\text{Adsorption capacity}(q_e) = \frac{C_0 - C_e}{m} \times V \quad (2)$$

$$\text{Adsorption efficiency} = \frac{C_0 - C_e}{C_0} \times 100\% \quad (3)$$

C_0 and C_e are the initial and equilibrium concentration (ppm), m is the mass (g) of the adsorbent and V is the volume (L) of the solution containing solute.

Microplastics removal: Mimby AB (Gothenburg, Sweden) kindly donated the model microplastics dispersion in the form of a laundry effluent sample. The initial liquid sample contained bigger pieces of debris, therefore before proceeding with the separation experiments, the sample was sieved through a 1 mm mesh to ensure that all of the dispersed particles met the specification of microplastics stated in ISO/TR 21960:2020, i.e. their diameter was equal or below 1 mm. 100 mL of sieved liquid was then poured into a previously weighed, clean, and oven-dried beaker, and placed in a furnace at 100 °C to evaporate the water. The separation experiments were conducted on uniformly porous TCNF/PLA, ChNF/PLA and reference PLA filters of both geometries i.e. hourglass and cylindrical. The separation efficiency was measured by gravimetric method. 50 mL of microplastics solution was pushed through each filter with the use of a syringe, followed by a thorough rinse with deionized water for approximately 1 min. The filtrate solution was collected in an oven-dried pre-weighed beaker and placed in the furnace at 100 °C to evaporate water. The remaining debris was weighted and related to the weight of the starting microplastics content. To ensure experimental reproducibility, the presented results are an average of 5 experimental runs for each filter's design and material used.

Transmission Electron Microscopy (TEM): Bright-field TEM images were obtained using a JEM-2100F from JEOL operated at 200 kV using a Gatan Ultrascan camera with an exposure time of 1 s. The TCNF solution (0.001 %) was drop-casted onto a glow-discharged carbon-coated copper grid (EMS CF150-Cu-UL). The characterisation of the final 3D printed TCNF/PLA filter, an internal part of the filter was first sectioned into 100 nm thickness using a Leica Ultracut UCT with a 45° diamond knife from Diatome and later transferred the same type of grid.

3. Results and discussion

3.1. Development of the biocomposite filaments

Homogenous dispersion of hydrophilic cellulose and chitin

nanofibers (NFs) in a hydrophobic PLA matrix is known to be challenging due to the NFs' polar surfaces, large surface area and high aspect ratio [55]; therefore various compatibilizers [56,57] are commonly added during the composite preparation process. However, this study shows that even without additional compatibilizers, the development of functional, well-dispersed biocomposites reinforced with 5 wt% of the NF of choice is possible, which can likely be attributed to the thermally induced phase separation (TIPS) pelletization step of the procedure.

The preparation of PLA-based biocomposites by physical blending followed by TIPS was reported in the previous work [34] on the development of fish scale-extracted hydroxyapatite (HAP)/PLA composite for water treatment applications. The pelletization of the biocomposite by the TIPS method showed to be an efficient route to enhance filler dispersion in the polymer matrix by utilizing the development of a well-interconnected polymer network [27]. In the previous study [34], a well-dispersed HAP/PLA biocomposite with 15 wt% of functional filler was obtained. However, in an attempt to improve the 3D printability of the composites, within this study, the development of two new formulations is presented. The spherical PLA biocomposite pellets reinforced with either TCNF or ChNF were formed upon dropwise addition of PLA/NF/ dioxane suspension into the liquid nitrogen (LN₂). The obtained pellets were instantly freeze-dried, followed by single-screw extrusion into 3D printing filaments (Fig. 1).

The extruded biocomposite 3D printing filaments showed surface texture and flexibility comparable to that of pure, commercial PLA filament, however differed in odour and colour. The desired application of the 3D printed filters is water treatment, therefore addition of adsorption functionality already at the filament-development stage is of essence. The choice of NFs ensured the addition of functional chemical groups i.e. COO⁻ for TCNF enabling adsorption of positively charged metal ions by electrostatic interactions [53]; as well as amide (–NHCO–) and amine (–NH₂) groups in case of ChNF with lone pair of electrons enabling adsorption by chelation [58].

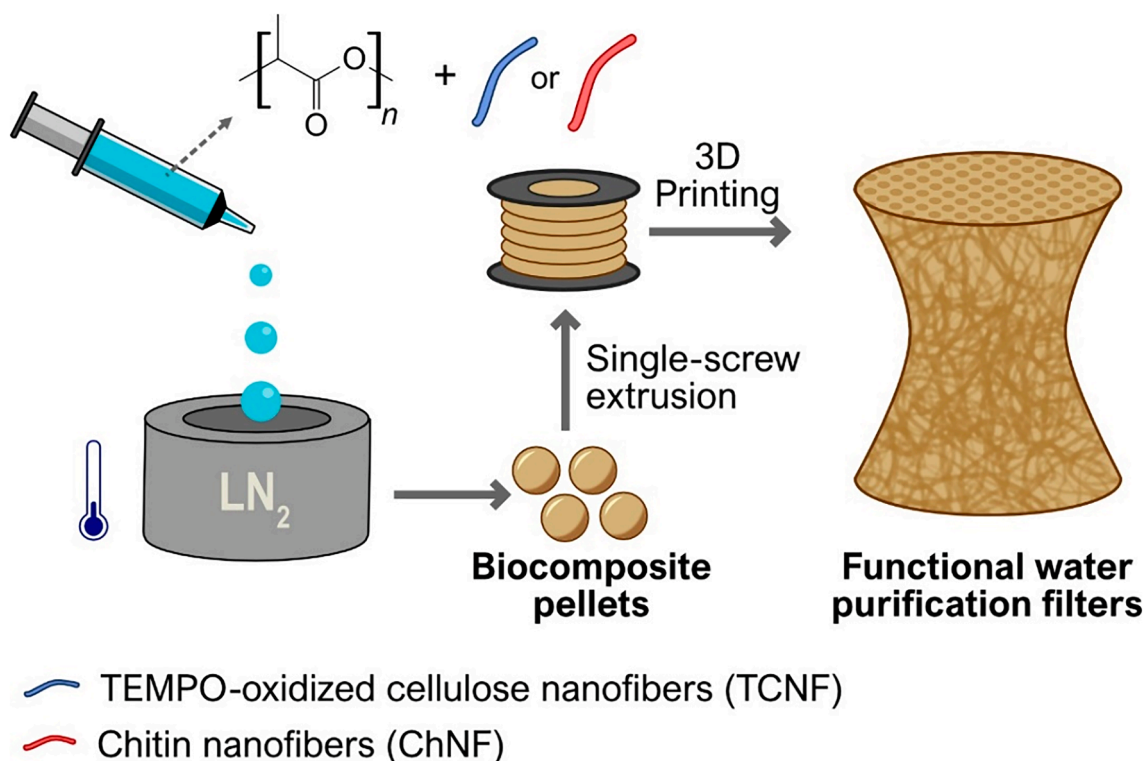


Fig. 1. Overview of the experimental procedure for processing the biocomposites, 3D printable filaments and the filters.

3.2. Characterization of the 3D printed models

3.2.1. 3D printing procedure

To ensure the precision of the 3D printing procedure and avoid nozzle obstruction, the printing temperatures for the biocomposite filaments were programmed 20 °C higher than for the reference PLA filament. The 3D printing procedure was smooth, and no clogging or disruption in the material flow was observed for neither of the biocomposite filaments, yielding high quality, and detailed prints (Fig. 2a-d). The designed and printed porous filters were either cylindrical or hourglass-shaped. The filters were designed to vary the contact time between different contaminants and different adsorbent nanospecies i.e. TCNF and ChNF, while maintaining steady and satisfactory permeance due to big pores.

3.2.2. Morphology and permeability of the 3D printed filters

The morphology of the synthesized biocomposite pellets as well as of all of the 3D printed porous filters was assessed with the use of the SEM (model size 10 × 10 × 10 mm). The pore size and shape, channel interconnectivity, and print quality were of main interest.

The morphology of all of the samples was tested within each experimental step (Fig. 2e). As observed by the SEM, both the pellets and filament cross-sections of the biocomposites do not differ from the reference PLA samples, as all of them exhibited homogenous and smooth surfaces. The pore size data (Table 1) and print quality of the filters confirmed what was observed by the naked eye, i.e. all of the filters show very high print quality with uninterrupted print pattern and consistency in terms of the line width and geometry of the designed pores. It was not possible to observe any inhomogeneity in the developed TCNF/PLA filters using high-resolution transmission electron microscopy (TEM) (Figure S4), which indicates a well dispersed NFs in the PLA matrix. As presented in Fig. 2f the presence of functional NFs is expected both

within the bulk of the filter's wall as well as on its surface.

It was shown that the 3D printing procedure induced shrinkage of the material, leading to actual pore sizes differing from the programmed ones (Table 1). Shrinkage of the programmed pore sizes in a porous model is a natural phenomenon occurring during 3D printing while using thermoplastic polymers due to temperature changes between the freshly extruded thermoplastic melt and cooled extruded layers [35]. The reference PLA filters were least affected by the shrinkage, as the actual porous structure of the 3D printed filter was very well maintained when compared to the programmed porosity architecture (i.e. biggest pores of the three-level gradient cylinder and the smallest pores of the two-level gradient hourglass-shaped model). However, in other cases, the actual pore sizes of the PLA filter were smaller than the programmed ones. The reduction of the pore size of uniformly porous cylinder and hourglass-shaped filter was 26 % and 19 %, respectively. For the gradient porosity cylindrical and hourglass-shaped filters, the reduction oscillated around 20 % and 8 %, respectively.

The effect of pore size shrinkage was more pronounced for both of the biocomposite samples. The pore size drop for the uniform cylinder filters was 27 % and 42 % for the TCNF/PLA and ChNF/PLA, respectively. For the gradient porosity cylinder, the average pore size reduction was 17 % for the TCNF/PLA and 19 % for the ChNF/PLA samples. The uniform and gradient hourglass-shaped samples exhibited pore size reduction of 27 % and 23 % for the TCNF/PLA and 24 % and 28 % for ChNF/PLA filters, respectively. In general, the pore size reduction for the composite samples was approximately the same range for all of the tested shapes which indicates that the relative pore size reduction is independent of the filter's design and depends on the type of NF added. The polymer chains orient themselves during the 3D printing process, and the shrinkage of the material is affected by whether the direction of the polymer's flow is parallel or perpendicular to the print bed. Hence, the addition of high aspect-ratio fillers such as TCNF or ChNF to the

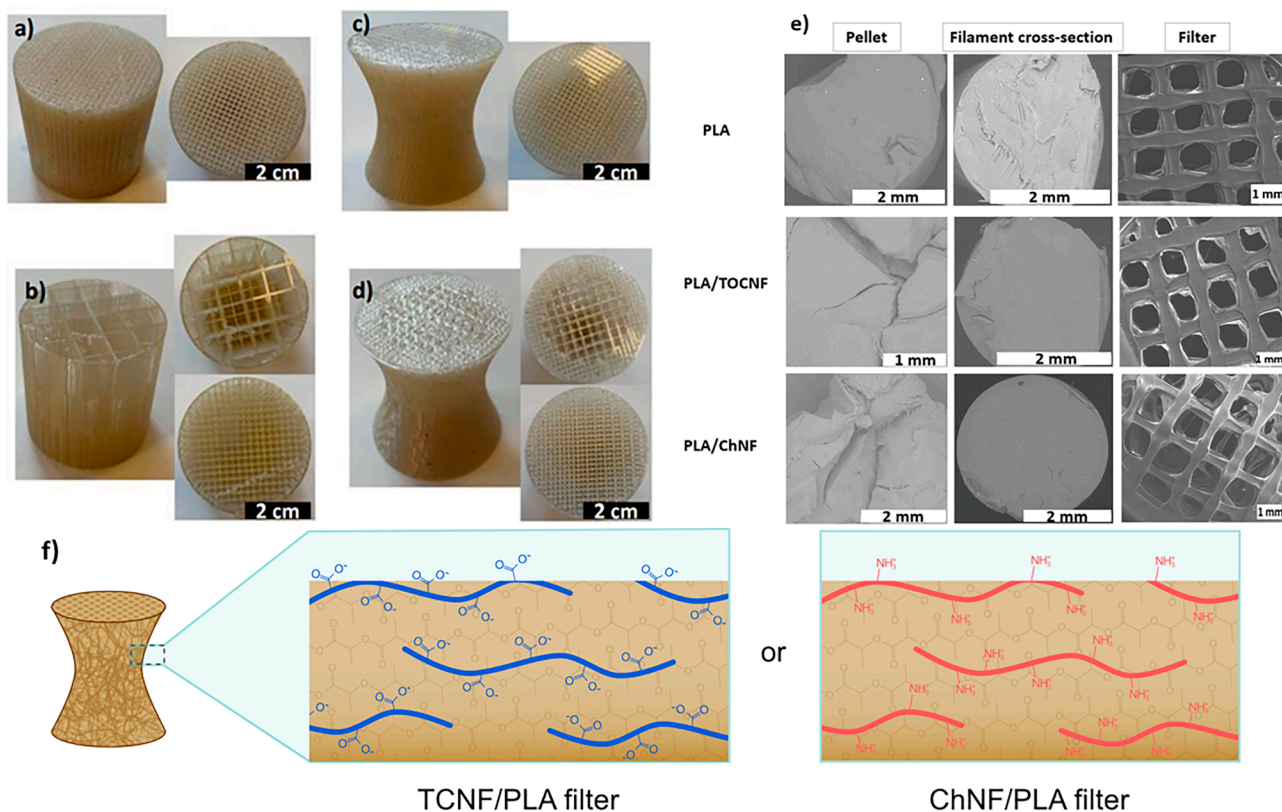



Fig. 2. 3D printed filter models a) uniform porosity cylinder, b) three-level gradient porosity cylinder, c) hourglass-shaped uniform porosity filter, d) hourglass shapes two-level gradient porosity filter, e) SEM images of each experimental step, i.e. pellet, filament and filters cross-section for the reference PLA and both the composite samples; f) graphic representation of dispersion of NFs on the filter's surface.

Table 1

Measured pore size and percent of shrinkage (%_{sh.}) of the 3D printed water purification filters.

Model	Porosity structure	Programmed pore size (mm)	PLA (mm)	TCNF/PLA (mm)	ChNF/PLA (mm)
	Uniform	1.5	1.12 ± 0.11 % _{sh.} = 25	1.09 ± 0.09 % _{sh.} = 27	0.87 ± 0.07 % _{sh.} = 37
	Three-level gradient	8	8.08 ± 0.47 % _{sh.} = 0	7.81 ± 0.02 % _{sh.} = 2	7.52 ± 0.50 % _{sh.} = 6
		4	3.20 ± 0.16 % _{sh.} = 20	3.13 ± 0.22 % _{sh.} = 22	3.09 ± 0.18 % _{sh.} = 23
		2	1.59 ± 0.05 % _{sh.} = 20	1.49 ± 0.06 % _{sh.} = 25	1.45 ± 0.08 % _{sh.} = 27
	Uniform	1.5	1.21 ± 0.09 % _{sh.} = 19	1.09 ± 0.10 % _{sh.} = 27	1.14 ± 0.10 % _{sh.} = 24
	Two-level gradient	3	2.76 ± 0.04 % _{sh.} = 8	2.35 ± 0.16 % _{sh.} = 22	2.11 ± 0.17 % _{sh.} = 30
		1.5	1.58 ± 0.04 % _{sh.} = 0	1.15 ± 0.09 % _{sh.} = 23	1.12 ± 0.10 % _{sh.} = 25

polymer matrix can somewhat disrupt the polymer chain orientation during melt and extrusion process leading to more pronounced shrinkage of the final porous 3D printed model [35,59]. Within this work, in most 3D printed designs, there was no big difference in pore size shrinkage between the two NFs used, however ChNF seems to induce bigger pore shrinkage when compared to the relative designs printed with the use of TCNF-reinforced filaments, hence indicating that ChNF presents slightly higher aspect ratio than the TCNF used. Another plausible explanation of this phenomenon is the impact of the biocomposite filaments' viscosity during the melting stage of the 3D printing process. Naturally, addition of both TCNF and ChNF NFs change the viscosity of the PLA filament. This, combined with higher printing temperature, which is essential for ensuring the high print quality of the biocomposite filters, leads to lower viscosity of the biocomposite material in the printers' heated chamber and consequently easier extrusion and flow through the heated nozzle. Therefore, easier and slightly faster deposition of the biocomposite material on the print bed could mean that more of the biocomposite material is being extruded and deposited when compared to the commercial PLA filament, which leads to thicker walls and in consequence smaller pore size. This observation would be expected to be more pronounced in absolute numbers for designs with smaller programmed pore sizes, hence it correlates well with the data collected in Table 1.

All of the structures exhibited excellent permeance values, as the relatively big pores enable a high rate of water transport through the 3D printed filters. In a first approximation, we accounted for most of the pressure loss to the inlet and outlet tubes (4 mm hydraulic diameter), which expanded to the 40 mm filter diameter just upstream of the filter. The resulting uneven flow distribution, i.e., higher flow rate at the centre and lower flow rate at the outer diameter, will affect the pressure loss and pollutant adsorption. Therefore, adsorption studies were conducted in steady-state on immersed filters. Microplastics retention is less

impacted by the uneven flow-distribution given that the main reason is size exclusion on the filter surface. Additionally, the microplastics debris on the filter can increase the total pressure loss and even the flow upstream of the filter improving the performance. The high permeance measured, under consideration that the filter itself only marginally contributed to the resistance, proves its applicability and employment without the contribution of higher driving pressures.

3.2.3. Mechanical properties

PLA, TCNF/PLA, and ChNF/PLA 3D printed filters, with uniform and gradient porous structures, were subjected to uniaxial compression tests. The reinforcing effect of the TCNF and ChNF on the PLA matrix as well as the effect of different porosity architectures on the mechanical properties of the filters was studied. Representative stress-strain curves are shown in Fig. 3a from where it is possible to distinguish three different stages of compressive deformation for all the prototypes [60]. Fig. 3b shows the first stage of compressive deformation. This region of the curve showed a linear elastic behaviour for all of the samples and was used to determine the apparent compressive elastic modulus (calculated values for all tested specimens are presented in Table S3).

When comparing the samples with uniform porosity against the filters with gradient porosity (Fig. 3c), it was possible to observe major differences in their behaviour. The collapse of the uniformly porous structure was initiated in the middle of the filter and spread along the z-axis for as long as the uniaxial compression force was applied. This behaviour i.e. bending of the structural walls of the filters is represented in Fig. 3b. The calculated apparent compressive elastic modulus for TCNF/PLA samples was 3 % higher than for the PLA, while for ChNF/PLA it was 7 % lower (Fig. 3d).

The improvement of compressive elastic modulus for uniformly porous samples had no significant statistical value, however, the gradient porosity structures exhibited a more pronounced enhancement of mechanical properties. When analysing the results of the gradient porosity samples, the first section of the curve, represented in Fig. 3a (and zoomed-in in Fig. 3b), is the result of the bending of the walls where the larger pores are situated (refer to Fig. 3c for the differences in pore structure). For these particular samples, it was possible to observe two different behaviours. For PLA samples the section with the larger pores, was completely bent, while the smaller pore-size section was unaffected by the compression force. Nevertheless, for both TCNF/PLA and ChNF/PLA, the bigger pore sized section was affected at the beginning, and then followed by the bending of the smaller pore size section. This resulted in apparent compressive elastic modulus values that were 13 % and 28 % higher for TCNF/PLA and ChNF/PLA, respectively, than for the reference PLA (Fig. 3d). This can be an indication of the impact of porous architecture on the final properties of the 3D printed filters.

The second region of the curves represented in Fig. 3a or the "plateau region" of the curves, presented the full collapse of the walls. In the case of the uniformly porous structure, a rise of stress values after this plateau region was observed. This is considered to be the densification regime, which is characteristic for the walls that approach each other and touch. Contrary to this behaviour, in the case of the gradient porous structure, the rise of the stress values defined the compressive strain at which the wall from the smaller-pored section started bending. It continued until reaching a new maximum, and then decreased as the bent walls collapse. Although this behaviour is interesting and quite characteristic of the gradient structures, for practical applications its values are not of much importance since in working conditions, the filter would be permanently damaged after the first region of the curve and thus higher stress ought to be avoided.

Furthermore, for the desired application, the energy dissipation i.e. toughness, is the most important parameter in terms of mechanical properties. This was calculated considering the area under the stress vs strain curve. As shown in Fig. 3d, for both uniform and gradient structures, the addition of TCNF and ChNF improved the energy absorption

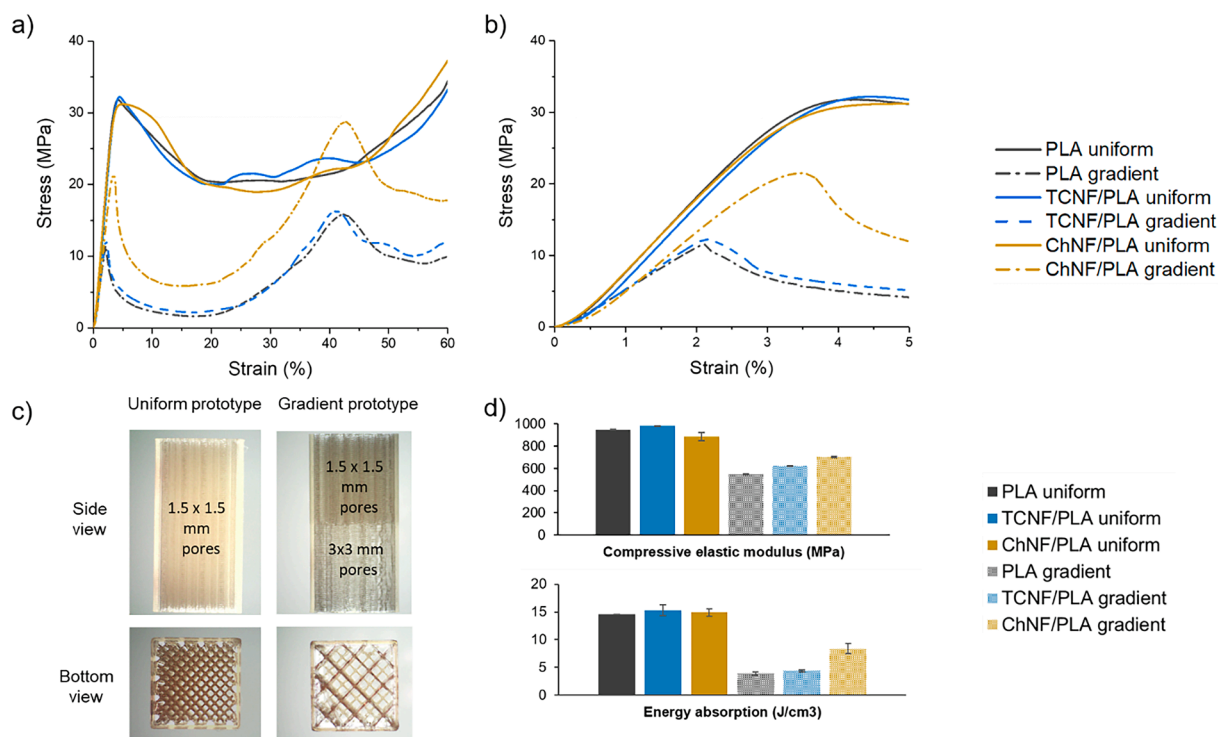


Fig. 3. a) Stress–strain curves of all of the tested samples, b) Elastic behaviour stage of the stress–strain curves presented in a), c) microscope overview of the compression test sample, d) compressive elastic modulus and energy absorption of all of the samples.

values. The most interesting behaviour was observed for ChNF/PLA with gradient pores, with the energy dissipation value being 117 % higher than its equivalent in PLA. Moreover, the gradient ChNF/PLA sample exhibited high compressive modulus value, which together with the obtained toughness values, indicate achieving a great balance between stiffness and toughness [61]. This behaviour is not commonly observed for PLA, which is normally characterised as a very brittle material [62]. Nevertheless, higher values of compressive elastic modulus and toughness were observed for samples with uniform pore structures, which had smaller pores, hence larger wall thickness compared to the gradient structures. The biggest improvement in the mechanical performance of filters was however observed for samples with gradient arrangement of pores, which shows great potential of implementing tuneable porosity structures into water filtration systems.

Ultimately, the good mechanical properties and structural resistance of the TCNF/PLA and ChNF/PLA porous filters were considered favourable for use in the water treatment industry. The enhancement of mechanical properties is assigned to the synergistic effect of both tailored pore architecture and overall design of the 3D printed filters as well as of homogenous dispersion of NF in the plastic matrix acting as a reinforcement, which supports previous indicative TEM observations (Figure S4).

3.2.4. Functionality of the 3D printed filters: Cu (II) adsorption and microplastics removal by size exclusion

The adsorption performance of the 3D printed PLA-based filters reinforced with either TCNF or ChNF was assessed via a batch adsorption study with the use of Cu^{2+} ions. As the adsorption capabilities of the filters were not tested under direct water flux due to limitations of the in-house constructed setup resulting in uneven flow distribution, the permeance was not taken into consideration and the hourglass-shaped filter with uniform porosity structure was used as the model filter. The obtained results summarizing the maximum adsorption capacity and maximum adsorption efficiency of three different filters (i.e. TCNF/PLA, ChNF/PLA, and reference PLA filter) in two differently concentrated

solutions are summarized in Fig. 4.

As expected, the highest adsorption capabilities for all the filters and both of the concentrations were observed during the initial adsorption cycle. For the 1 mM solution, the maximum adsorption efficiency was achieved by ChNF/PLA filters with almost 51 %, followed by TCNF/PLA with 47 % removal efficiency. Both composites showed a significant increment in the maximum removal efficiency over the reference PLA filter that was oscillating around 11 %. The calculated maximum adsorption capacity was 88 and 90 mg/g_{NF} for ChNF/PLA and TCNF/PLA filters, respectively, compared to 10 mg/g for the reference PLA filter. The adsorption capacity increased with the initial concentration of the metal solution (i.e. at 10 mM) reaching 208 mg/g_{NF} (10.4 mg/g_{filter}) and 234 mg/g_{NF} (12.6 mg/g_{filter}) for ChNF/PLA and TCNF/PLA filters, respectively. Compared to the adsorption capacity of the reference PLA filter (4 mg/g), this shows the great potential of the developed 3D filters for the removal of copper ions from the aqueous medium. The obtained results clearly indicate the presence of NFs, not only as a reinforcement within the bulk of the filaments and filters but also on the surface of the filters, as illustrated on Fig. 2f. However, the role of PLA in the adsorption process should not be overlooked. The adsorption capacities are presented per g of NFs in the filters, however PLA enhances adsorption. Plastics are considered inert; however previous studies report sorption of metal ions onto various plastics, including PLA [63]. Moreover, the pH of adsorption is above PLA's point of zero charge (pH_{pzc}), hence the filter's surfaces become negatively charged (as shown by zeta potential results presented in Figure S5) and prone to attracting positively charged Cu^{2+} ions [58,63].

Both the adsorption mechanism and adsorption kinetics of various metal ions onto cellulose [64–67] and chitin [58] - based materials were previously broadly reported in the literature, hence we do not expect different adsorption mechanisms to occur. The adsorption of metal ions onto the chitin surface occurs via coordination and formation of stable complexes between the metal ions and amino sugars of chitin [68,69]. The lone pair at amino and N-acetyl amino groups can bond with transition metal ions [68]. Moreover, deprotonated hydroxyl groups can

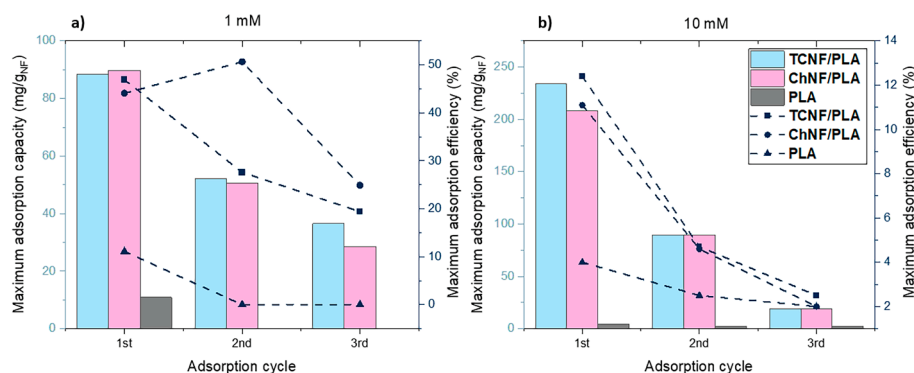


Fig. 4. Adsorption capacity and efficiency of the filters as tested in a) 1 mM and b) 10 mM copper sulfate solutions at pH = 6–7.5.

form bonds with metal ions via coordination [68]. For oxidized cellulose and chitin, respectively, Sehaqui et al. [54] studied the adsorption of Cu^{2+} ions onto oxidized cellulose and chitin NFs and showed that the adsorption increases linearly with carboxylate content for pH 3 and 7 with maximum adsorption capacities of 135 and 55 mg/g. It was established that Cu^{2+} ions are adsorbed onto the TCNF via electrostatic interactions involving the carboxyl groups on the oxidized cellulose fiber surface [64]. The proton of the carboxyl group is exchanged with a metal ion during the adsorption process. Liu et al. [53] studied the mechanism of adsorption of copper ions onto pure TCNF and suggested that the Cu^{2+} ions are first adsorbed by the carboxylic groups on the TCNF, and then gradually reduced and self-assembled to Cu (0) or copper oxide nanoparticles by microprecipitation.

3.2.5. Recyclability and reusability of the 3D printed filters

The recyclability potential of the 3D printed filters was evaluated showing that the maximum adsorption efficiency drops by approximately 50 % after the first adsorption cycle and another 30 % after the

second adsorption cycle for both of the biocomposite materials. It is therefore highly recommended to explore other potential uses of the filters after the first adsorption cycle is completed and the adsorbed metal ions are desorbed. Thus, it was proposed to further utilize the unique potential of the tuned porosity architecture of the filters. The filters were used for the separation of debris from contaminated laundry water samples via size exclusion, enhanced by physical interactions between the filters' surface and debris particles. An actual laundry sample collected from a shared laundromat was used to test the potential of the filters for removal of debris, further referred to as microplastics. The laundry effluent itself was not analytically tested, therefore it could contain inorganic particles and contaminants of other origin as well as microplastics, however for the experimental purposes we treated the contaminated water as a model containing solely microplastics. Within this study, it was established that 1 L of laundry water contains approximately 195 mg of fibre residues i.e. microplastics. It is estimated that a single wash cycle consumes approximately 60 L of water [70], meaning that up to 12 g of microplastics are released into the

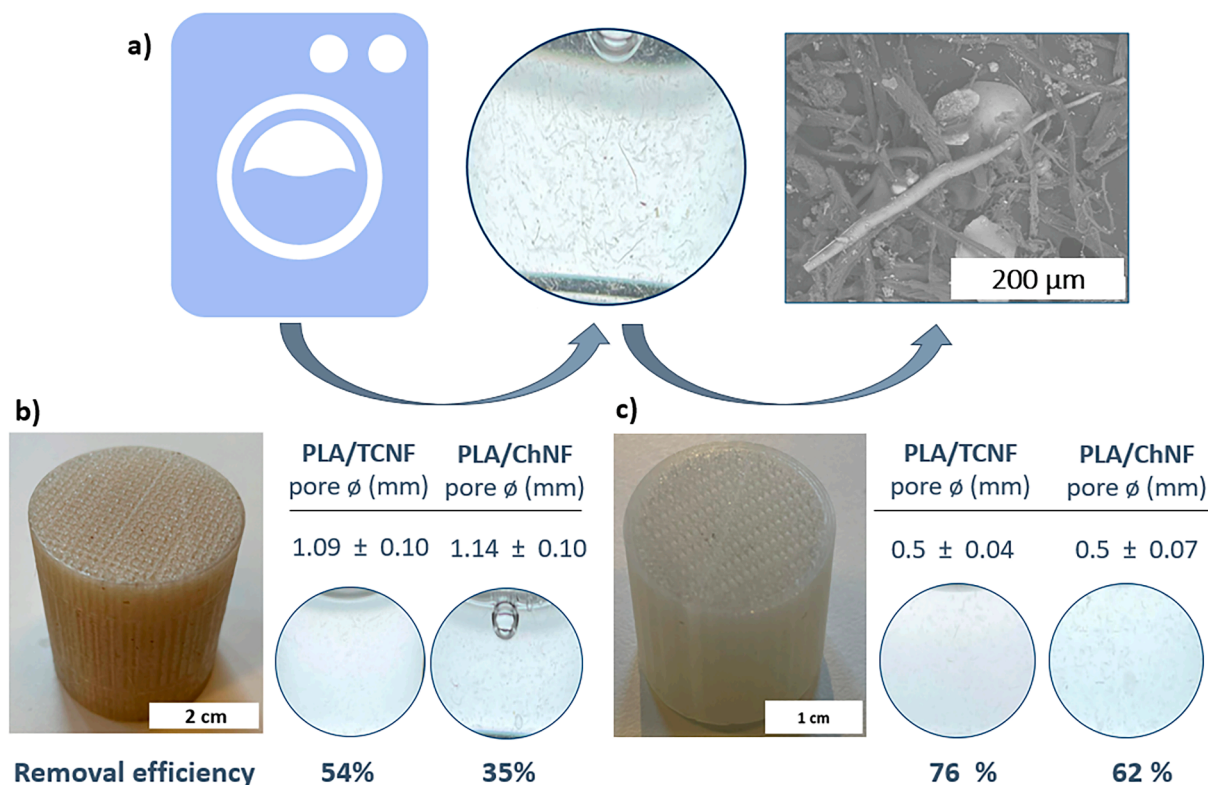


Fig. 5. a) Microplastics solution collected from laundry and SEM image of the particles, and average pore diameter and microplastics removal efficiency of b) filters with programmed pore size of 1 mm and c) programmed pore size of 0.5 mm.

environment with each wash cycle. Considering, that each day there are thousands of wash cycles occurring all over the world, it can be estimated that the daily release of microplastics from laundry machines reaches tens of tons. This estimation is based on microplastics particles, which are smaller than 1 mm in their biggest diameter, and does not take into consideration particles often reported as microplastics in the size range between 1 and 5 mm [71]. Expanding the size definition of the microplastics means that there are hundreds of tons of petroleum-based particles released into the environment daily from washing machines alone.

The microplastics debris in the test water was visible to the naked eye. Microplastics were present in various shapes, sizes, and forms, ranging from elongated fibrils of up to 0.9 – 1 mm in size to smaller dot-like particles and clusters with diameters smaller than 100 μm (See Fig. 5a). Two different filter designs were tested for the removal of microplastics i.e. hourglass and cylindrical filters with uniform porous structures.

The average removal efficiency (as tested for 10 samples per measurement) of microplastics for the ChNF/PLA filters was 35 % for both of the geometries, whereas for the TCNF/PLA filters it was 40 % for the hourglass and 54 % for the cylindrical filter. The influence of the NFs, especially in the case of the TCNF/PLA filter, is evident, as the average removal efficiency for the reference PLA filters is 26 % for the cylindrical and 29 % for the hourglass-shaped filter. The microplastics retained on the filter surface were stably deposited and retained whilst washing the filter with 1 L of deionized water, observed visibly by eye, proving the permanent removal of microplastics from the effluent without compromising their permeance.

After filtering the microplastics solution through 3D printed filters, the reduction of the microplastics concentration was evident since the filtrate solution was less turbid. Most of the elongated fibril-like species were effectively stopped, irrespective of the filter's shape and bio-composite used for 3D printing (Fig. 5). The filtrate collected using the reference PLA filter showed much more debris than either of the bio-composite filters, which strongly indicates the participation of the NFs in the filtration process and their impact on the overall pore size of the filters [72]. This interaction potentially occurs via formation of stronger physical bonds between the filter's reinforcing nanospecies and microplastics particles compared to interactions between PLA with speculated lower chances of the microplastics slipping off the filter during retention. Further, the particles not removed at the initial retention filtration, for example, particles being smaller than the pore size, can be removed by adhesion to the filter wall. The fact that removal is affected by the presence of the NFs points towards chemical interactions in addition to mechanical sieving. This phenomenon and related mechanisms, however, needs to be evaluated systematically using model water systems and will be done in a separate study.

The separation process could be repeated with a similar efficiency many times – 10 times successful repetition on the lab scale – by simply rinsing filters thoroughly with deionized water for several minutes and recovering the leftover residues. This allows a simple route for the collection and further treatment and/or appropriate disposal of the microplastics collected. As a follow-up experiment carried out within this work, the prototype filters in hourglass and cylindrical form with uniform porosity structure with an average pore size of 500 μm were 3D printed and tested for microplastics separation efficiency. Whilst the permeability drops with the pore size, the removal efficiency (by retention at the filter inlet and possible adhesion at the larger specific surface) increases on average by 75 % and 60 % for the TCNF/PLA and ChNF/PLA filters of both shapes, respectively (Fig. 5c). All of the filters with a programmed pore size of 0.5 mm are presented in Figure S6. In a future investigation, the gradual reducing cross-section for retention filtration will be further explored.

4. Conclusions

Two different PLA-based biocomposites reinforced with 5 wt% of either TCNF or ChNF were developed by physical blending, followed by TIPS, and 3D printed in cylindrical and hourglass-shaped designs of multiscale porosity architectures. The 3D printed filters exhibited a very high surface-finish quality and consistency in both pore shape and channel interconnectivity throughout the entire length of the filters, irrespective of their geometry, porous design and materials used for 3D printing.

The 3D printed filters showed great permeance, high compressive strength, and improved toughness values when compared to pure PLA filters. Moreover, they proved to be functional for the adsorption of copper ions from a contaminated aqueous medium on the lab scale as well as for the separation of microplastics from laundry effluent water. The adsorption of metal ions was attributed to electrostatic interactions between the NFs dispersed and PLA itself and copper ions, whereas the microplastics removal occurred primarily via size-exclusion enhanced by physical bonding of particles onto the filters' surface. The filters can be recycled, by initially being utilized for the adsorption of metal ions and then, after desorption and safe collection of metal ions, being reused multiple times for the removal of microplastics from contaminated laundry water.

The ease of processing of the developed biocomposite filaments via 3D printing indicates their high commercialization potential for low-cost, custom production of durable filtration systems easily available at the point of need. The increased accessibility of the nanoentities on the filters' surface as well as further surface functionalization by chemical or physical treatments to tailor the filters for specific application requirements, can be the scope of future studies.

Declaration of Competing Interest

The authors declare that they have no known competing financial interests or personal relationships that could have appeared to influence the work reported in this paper.

Data availability

Data will be made available on request.

Acknowledgments

This work was funded by Knut and Alice Wallenberg Foundation (Wallenberg Wood Science Center) and the Swedish Foundation for Strategic Environmental Research (Mistra), project MISTRA TerraClean (project no. 2015/31). The authors wish to thank Add North 3D AB, Ölsremma, Sweden for their help with the filament extrusion and Mimby AB, Gothenburg, Sweden for providing the laundry water sample. We thank Dr. Jing Li for analysing the size of chitin nanofibers with AFM. We thank Dr. Tom Willhammar and Mathias Nero for TEM measurements.

Appendix A. Supplementary data

Supplementary data to this article can be found online at <https://doi.org/10.1016/j.cej.2022.141153>.

References

- [1] V. Kumar, R.D. Parihar, A. Sharma, P. Bakshi, G.P. Singh Sidhu, A.S. Bali, I. Karaouzas, R. Bhardwaj, A.K. Thukral, Y. Gyasi-Agyei, J. Rodrigo-Comino, Global evaluation of heavy metal content in surface water bodies: a meta-analysis using heavy metal pollution indices and multivariate statistical analyses, *Chemosphere* 236 (2019) 124364, <https://doi.org/10.1016/j.chemosphere.2019.124364>.
- [2] A.A. Koelmans, N.H. Mohamed Nor, E. Hermesen, M. Kooi, S.M. Mintenig, J. De France, Microplastics in freshwaters and drinking water: critical review and

- assessment of data quality, *Water Res.* 155 (2019) 410–422, <https://doi.org/10.1016/j.watres.2019.02.054>.
- [3] 14:00-17:00, ISO/TR 21960:2020, ISO. (n.d.). <https://www.iso.org/cms/render/live/en/sites/isoorg/contents/data/standard/07/23/72300.html> (accessed October 20, 2022).
- [4] A. Boulamanti, J.A. Moya, Production costs of the non-ferrous metals in the EU and other countries: copper and zinc, *Resour. Policy* 49 (2016) 112–118, <https://doi.org/10.1016/j.resourpol.2016.04.011>.
- [5] G. Izydorczyk, K. Mikula, D. Skrzypczak, K. Moustakas, A. Witek-Krowiak, K. Chojnacka, Potential environmental pollution from copper metallurgy and methods of management, *Environ. Res.* 197 (2021), 111050, <https://doi.org/10.1016/j.envres.2021.111050>.
- [6] S.J. Markich, R.A. Jeffree, P.T. Burke, Freshwater bivalve shells as archival indicators of metal pollution from a copper–uranium mine in tropical Northern Australia, *Environ. Sci. Technol.* 36 (2002) 821–832, <https://doi.org/10.1021/es011066c>.
- [7] Y. Wang, R. Wang, L. Fan, T. Chen, Y. Bai, Q. Yu, Y. Liu, Assessment of multiple exposure to chemical elements and health risks among residents near Huodehong lead-zinc mining area in Yunnan, Southwest China, *Chemosphere* 174 (2017) 613–627, <https://doi.org/10.1016/j.chemosphere.2017.01.055>.
- [8] P. Bhatt, V.M. Pathak, A.R. Bagheri, M. Bilal, Microplastic contaminants in the aqueous environment, fate, toxicity consequences, and remediation strategies, *Environ. Res.* 200 (2021), 111762, <https://doi.org/10.1016/j.envres.2021.111762>.
- [9] A. Galvão, M. Aleixo, H. De Pablo, C. Lopes, J. Raimundo, Microplastics in wastewater: microfiber emissions from common household laundry, *Environ. Sci. Pollut. Res.* 27 (2020) 26643–26649, <https://doi.org/10.1007/s11356-020-08765-6>.
- [10] A.P.M. Velenturf, P. Purnell, Principles for a sustainable circular economy, *Sustain. Prod. Consumpt.* 27 (2021) 1437–1457, <https://doi.org/10.1016/j.spc.2021.02.018>.
- [11] L.-T. Lim, R. Auras, M. Rubino, Processing technologies for poly(lactic acid), *Prog. Polym. Sci.* 33 (2008) 820–852, <https://doi.org/10.1016/j.progpolymsci.2008.05.004>.
- [12] D. Klemm, B. Heublein, H.-P. Fink, A. Bohn, Cellulose: fascinating biopolymer and sustainable raw material, *Angew. Chem. Int. Ed.* 44 (2005) 3358–3393, <https://doi.org/10.1002/anie.200460587>.
- [13] C. Peniche, W. Argüelles-Monol, F.M. Goycoolea, Chapter 25 - Chitin and Chitosan: Major Sources, Properties and Applications, in: M.N. Belgacem, A. Gandini (Eds.), *Monomers, Polymers and Composites from Renewable Resources*, Elsevier, Amsterdam, 2008, pp. 517–542, <https://doi.org/10.1016/B978-0-08-045316-3.00025-9>.
- [14] J.Y. Zhu, R. Sabo, X. Luo, Integrated production of nano-fibrillated cellulose and cellulosic biofuel (ethanol) by enzymatic fractionation of wood fibers, *Green Chem.* 13 (2011) 1339–1344, <https://doi.org/10.1039/C1GC15103G>.
- [15] A. Chakraborty, M. Sain, M. Kortschot, Cellulose microfibrils: A novel method of preparation using high shear refining and cryocrushing, 59 (2005) 102–107, <https://doi.org/10.1515/HF.2005.016>.
- [16] C.S.R. Freire, A.J.D. Silvestre, C.P. Neto, A. Gandini, L. Martin, I. Mondragon, Composites based on acylated cellulose fibers and low-density polyethylene: effect of the fiber content, degree of substitution and fatty acid chain length on final properties, *Compos. Sci. Technol.* 68 (2008) 3358–3364, <https://doi.org/10.1016/j.compscitech.2008.09.008>.
- [17] F.A. dos Santos, G.C.V. Iulianelli, M.I.B. Tavares, The use of cellulose nanofillers in obtaining polymer nanocomposites: properties, processing, and applications, *Mater. Sci. Appl.* 7 (2016) 257–294, <https://doi.org/10.4236/msa.2016.75026>.
- [18] M.U. Wahit, N.I. Akos, W.A. Laftah, Influence of natural fibers on the mechanical properties and biodegradation of poly(lactic acid) and poly(ϵ -caprolactone) composites: a review, *Polym. Compos.* 33 (2012) 1045–1053, <https://doi.org/10.1002/pc.22249>.
- [19] Z. Wang, J. Xu, Y. Lu, L. Hu, Y. Fan, J. Ma, X. Zhou, Preparation of 3D printable micro/nanocellulose-poly(lactic acid) (MNC/PLA) composite wire rods with high MNC constitution, *Ind. Crop. Prod.* 109 (2017) 889–896, <https://doi.org/10.1016/j.indcrop.2017.09.061>.
- [20] Q. Zhang, H. Lei, H. Cai, X. Han, X. Lin, M. Qian, Y. Zhao, E. Huo, E.M. Villota, W. Mateo, Improvement on the properties of microcrystalline cellulose/poly(lactic acid) composites by using activated biochar, *J. Clean. Prod.* 252 (2020), 119898, <https://doi.org/10.1016/j.jclepro.2019.119898>.
- [21] H. Nasution, N.G. Olaiya, M.K.M. Haafiz, C.K. Abdullah, S.A. Bakar, F.G. Olaiya, A. Mohamed, A.K. H. P. S., The role of amphiphilic chitosan in hybrid nanocellulose-reinforced poly(lactic acid) biocomposite, *Polym. Adv. Technol.* 32 (2021) 3446–3457, <https://doi.org/10.1002/pat.5355>.
- [22] C.M. Clarkson, S.M. El Awad Azrak, R. Chowdhury, S.N. Shuvo, J. Snyder, G. Schueneman, V. Ortalan, J.P. Youngblood, Melt spinning of cellulose nanofibril/poly(lactic acid) (CNF/PLA) composite fibers for high stiffness, *ACS Appl. Polym. Mater.* 1 (2019) 160–168, <https://doi.org/10.1021/acsapm.8b00030>.
- [23] J. Dong, M. Li, L. Zhou, S. Lee, C. Mei, X. Xu, Q. Wu, The influence of grafted cellulose nanofibers and postextrusion annealing treatment on selected properties of poly(lactic acid) filaments for 3D printing, *J. Polym. Sci. B* 55 (2017) 847–855, <https://doi.org/10.1002/polb.24333>.
- [24] H. Almasi, B. Ghanbarzadeh, J. Dehghannia, A.A. Entezami, A.K. Asl, Novel nanocomposites based on fatty acid modified cellulose nanofibers/poly(lactic acid): morphological and physical properties, *Food Packaging Shelf Life* 5 (2015) 21–31, <https://doi.org/10.1016/j.fpsl.2015.04.003>.
- [25] M. Jonoobi, A.P. Mathew, M.M. Abdi, M.D. Makinejad, K. Oksman, A comparison of modified and unmodified cellulose nanofiber reinforced poly(lactic acid) (PLA) prepared by twin screw extrusion, *J. Polym. Environ.* 20 (2012) 991–997, <https://doi.org/10.1007/s10924-012-0503-9>.
- [26] N.G. Olaiya, O.S. Obaseki, G.A.M. Mersal, M.M. Ibrahim, M.M. Hessian, O.F. Grace, A. Afzal, T. Khanam, A. Rashedi, Functional miscibility and thermomechanical properties enhancement of substituted phthalic acetylated modified chitin filler in biopolymer composite, *Royal Society Open Sci.* 9 (n.d.) 211411, <https://doi.org/10.1098/rsos.211411>.
- [27] G. Conoscenti, V.L. Carrubba, V. Brucato, A versatile technique to produce porous polymeric scaffolds: the thermally induced phase separation (TIPS) method, *Arch. Chem. Res.* 01 (2017), <https://doi.org/10.21767/2572-4657.100012>.
- [28] R. Zeinali, L.J. del Valle, J. Torras, J. Puiggali, Recent progress on biodegradable tissue engineering scaffolds prepared by thermally-induced phase separation (TIPS), *Int. J. Mol. Sci.* 22 (2021) 3504, <https://doi.org/10.3390/ijms22073504>.
- [29] E. Díaz, A.L. Molpeceres, I. Sandois, I. Puerto, PLLA/nHA composite films and scaffolds for medical implants: in vitro degradation, thermal and mechanical properties, *J. Inorg. Organomet. Polym.* 29 (2019) 121–131, <https://doi.org/10.1007/s10904-018-0972-y>.
- [30] K.-Y. Lee, J.J. Blaker, A. Bismarck, Surface functionalisation of bacterial cellulose as the route to produce green poly(lactide) nanocomposites with improved properties, *Compos. Sci. Technol.* 69 (2009) 2724–2733, <https://doi.org/10.1016/j.compscitech.2009.08.016>.
- [31] S. Sultan, N. Thomas, M. Varghese, Y. Dalvi, S. Joy, S. Hall, A.P. Mathew, The design of 3D-printed polylactic acid-bioglass composite scaffold: a potential implant material for bone tissue engineering, *Molecules* 27 (2022) 7214, <https://doi.org/10.3390/molecules27217214>.
- [32] A.-M. Yousefi, J. Liu, R. Sheppard, S. Koo, J. Silverstein, J. Zhang, P.F. James, I.-optimal design of hierarchical 3D scaffolds produced by combining additive manufacturing and thermally induced phase separation, *ACS Appl. Bio Mater.* 2 (2019) 685–696, <https://doi.org/10.1021/acsabm.8b00534>.
- [33] L. Zhu, S. Chen, K. Liu, W. Wen, L. Lu, S. Ding, C. Zhou, B. Luo, 3D poly (L-lactide)/chitosan micro/nano fibrous scaffolds functionalized with quercetin-polydopamine for enhanced osteogenic and anti-inflammatory activities, *Chem. Eng. J.* 391 (2020), 123524, <https://doi.org/10.1016/j.cej.2019.123524>.
- [34] N. Fijol, H.N. Abdelhamid, B. Pillai, S.A. Hall, N. Thomas, A.P. Mathew, 3D-printed monolithic biofilters based on a polylactic acid (PLA) – hydroxyapatite (HAp) composite for heavy metal removal from an aqueous medium, *RSC Adv.* 11 (2021) 32408–32418, <https://doi.org/10.1039/D1RA05202K>.
- [35] I. Gibson, D. Rosen, B. Stucker, M. Khorasani, in: *Additive Manufacturing Technologies*, Springer International Publishing, Cham, 2021, <https://doi.org/10.1007/978-3-030-56127-7>.
- [36] V. Mazzanti, L. Malagutti, F. Mollica, FDM 3D printing of polymers containing natural fillers: a review of their mechanical properties, *Polymers* 11 (2019) 1094, <https://doi.org/10.3390/polym11071094>.
- [37] Z. He, T.S. Shanmugasundaram, G. Singh, Inkjet 3D printing of clay ceramics for water treatment, *Prog. Addit. Manuf.* 3 (2018) 215–219, <https://doi.org/10.1007/s40964-018-0055-1>.
- [38] T. Luukkonen, J. Yliniemi, H. Sreenivasan, K. Ohenoja, M. Finnilä, G. Franchin, P. Colombo, Ag- or Cu-modified geopolymer filters for water treatment manufactured by 3D printing, direct foaming, or granulation, *Sci. Rep.* 10 (2020) 7233, <https://doi.org/10.1038/s41598-020-64228-5>.
- [39] L.D. Tijing, J.R.C. Dizon, I. Ibrahim, A.R.N. Nisay, H.K. Shon, R.C. Advincula, 3D printing for membrane separation, desalination and water treatment, *Appl. Mater. Today* 18 (2020), 100486, <https://doi.org/10.1016/j.apmt.2019.100486>.
- [40] N. Fijol, A. Aguilar-Sánchez, A.P. Mathew, 3D-printable biopolymer-based materials for water treatment: a review, *Chem. Eng. J.* 430 (2022), 132964, <https://doi.org/10.1016/j.cej.2021.132964>.
- [41] K. Kim, M.C. Ratri, G. Choe, M. Nam, D. Cho, K. Shin, Three-dimensional, printed water-filtration system for economical, on-site arsenic removal, *PLoS One* 15 (2020) e0231475, <https://doi.org/10.1371/journal.pone.0231475>.
- [42] Z. Shi, C. Xu, F. Chen, Y. Wang, L. Li, Q. Meng, R. Zhang, Renewable metal-organic-frameworks-coated 3D printing film for removal of malachite green, *RSC Adv.* 7 (2017) 49947–49952, <https://doi.org/10.1039/C7RA10912A>.
- [43] I.L. Liakos, A. Mondini, E. Del Dottore, C. Filippeschi, F. Pignatelli, B. Mazzolai, 3D printed composites from heat extruded polycaprolactone/sodium alginate filaments and their heavy metal adsorption properties, *Mater. Chem. Front.* 4 (2020) 2472–2483, <https://doi.org/10.1039/D0QM00159G>.
- [44] M. Shahbazi, H. Jäger, S.J. Ahmadi, M. Lacroix, Electron beam crosslinking of alginate/nanoclay ink to improve functional properties of 3D printed hydrogel for removing heavy metal ions, *Carbohydr. Polym.* 240 (2020), 116211, <https://doi.org/10.1016/j.carbpol.2020.116211>.
- [45] J.J. Koh, G.J.H. Lim, X. Zhou, X. Zhang, J. Ding, C. He, 3D-printed anti-fouling cellulose mesh for highly efficient oil/water separation applications, *ACS Appl. Mater. Interfaces* 11 (2019) 13787–13795, <https://doi.org/10.1021/acsami.9b01753>.
- [46] X. Li, H. Shan, W. Zhang, B. Li, 3D printed robust superhydrophilic and underwater superoleophobic composite membrane for high efficient oil/water separation, *Sep. Purif. Technol.* 237 (2020), 116324, <https://doi.org/10.1016/j.seppur.2019.116324>.
- [47] G.A. Appuhamillage, D.R. Berry, C.E. Benjamin, M.A. Luzuriaga, J.C. Reagan, J. J. Gassensmith, R.A. Smaldone, A biopolymer-based 3D printable hydrogel for toxic metal adsorption from water, *Polym. Int.* 68 (2019) 964–971, <https://doi.org/10.1002/pi.5787>.
- [48] L. Bergamonti, C. Bergonzi, C. Graiff, P.P. Lottici, R. Bettini, L. Elviri, 3D printed chitosan scaffolds: a new TiO₂ support for the photocatalytic degradation of amoxicillin in water, *Water Res.* 163 (2019), 114841, <https://doi.org/10.1016/j.watres.2019.07.008>.

- [49] D. Zhang, J. Xiao, Q. Guo, J. Yang, 3D-printed highly porous and reusable chitosan monoliths for Cu(II) removal, *J. Mater. Sci.* 54 (2019) 6728–6741, <https://doi.org/10.1007/s10853-019-03332-y>.
- [50] B. Jalvo, A. Aguilar-Sanchez, M.-X. Ruiz-Caldas, A.P. Mathew, Water filtration membranes based on non-woven cellulose fabrics: effect of nanopolysaccharide coatings on selective particle rejection, antifouling, and antibacterial properties, *Nanomaterials* 11 (2021) 1752, <https://doi.org/10.3390/nano11071752>.
- [51] H. Voisin, L. Bergström, P. Liu, A.P. Mathew, Nanocellulose-based materials for water purification, *Nanomaterials* 7 (2017) 57, <https://doi.org/10.3390/nano7030057>.
- [52] A. Aguilar-Sanchez, B. Jalvo, A. Mautner, S. Nameer, T. Pöhler, T. Tammelin, A. P. Mathew, Waterborne nanocellulose coatings for improving the antifouling and antibacterial properties of polyethersulfone membranes, *J. Membr. Sci.* 620 (2021), 118842, <https://doi.org/10.1016/j.memsci.2020.118842>.
- [53] P. Liu, K. Oksman, A.P. Mathew, Surface adsorption and self-assembly of Cu(II) ions on TEMPO-oxidized cellulose nanofibers in aqueous media, *J. Colloid Interface Sci.* 464 (2016) 175–182, <https://doi.org/10.1016/j.jcis.2015.11.033>.
- [54] H. Sehaqui, U.P. de Larraya, P. Liu, N. Pfenninger, A.P. Mathew, T. Zimmermann, P. Tingaut, Enhancing adsorption of heavy metal ions onto biobased nanofibers from waste pulp residues for application in wastewater treatment, *Cellulose* 21 (2014) 2831–2844, <https://doi.org/10.1007/s10570-014-0310-7>.
- [55] A. Isogai, L. Bergström, Preparation of cellulose nanofibers using green and sustainable chemistry, *Curr. Opin. Green Sustain. Chem.* 12 (2018) 15–21, <https://doi.org/10.1016/j.cogsc.2018.04.008>.
- [56] M. Kumar, S. Mohanty, S.K. Nayak, M. Rahail Parvaiz, Effect of glycidyl methacrylate (GMA) on the thermal, mechanical and morphological property of biodegradable PLA/PBAT blend and its nanocomposites, *Bioresour. Technol.* 101 (2010) 8406–8415, <https://doi.org/10.1016/j.biortech.2010.05.075>.
- [57] U.C. Paul, D. Fragouli, I.S. Bayer, A. Zych, A. Athanassiou, Effect of green plasticizer on the performance of microcrystalline cellulose/poly(lactic acid) biocomposites, *ACS Appl. Polym. Mater.* 3 (2021) 3071–3081, <https://doi.org/10.1021/acsapm.1c00281>.
- [58] P. Liu, H. Sehaqui, P. Tingaut, A. Wichser, K. Oksman, A.P. Mathew, Cellulose and chitin nanomaterials for capturing silver ions (Ag⁺) from water via surface adsorption, *Cellulose* 21 (2014) 449–461, <https://doi.org/10.1007/s10570-013-0139-5>.
- [59] M. Spoerker, J. Sapkota, G. Weingrill, T. Fischinger, F. Arbeiter, C. Holzer, Shrinkage and warpage optimization of expanded-perlite-filled polypropylene composites in extrusion-based additive manufacturing, *Macromol. Mater. Eng.* 302 (2017) 1700143, <https://doi.org/10.1002/mame.201700143>.
- [60] N. Lavoine, L. Bergström, Nanocellulose-based foams and aerogels: processing, properties, and applications, *J. Mater. Chem. A* 5 (2017) 16105–16117, <https://doi.org/10.1039/C7TA02807E>.
- [61] V. Nagarajan, A.K. Mohanty, M. Misra, Perspective on polylactic acid (PLA) based sustainable materials for durable applications: focus on toughness and heat resistance, *ACS Sustainable Chem. Eng.* 4 (2016) 2899–2916, <https://doi.org/10.1021/acssuschemeng.6b00321>.
- [62] J. Odent, J.-M. Raquez, P. Dubois, Highly Toughened Polylactide-Based Materials through Melt-Blending Techniques, in: *Biodegradable Polyesters*, John Wiley & Sons, Ltd, 2015: pp. 235–274. <https://doi.org/10.1002/9783527656950.ch10>.
- [63] F.G. Torres, D.C. Dioses-Salinas, C.I. Pizarro-Ortega, G.E. De-la-Torre, Sorption of chemical contaminants on degradable and non-degradable microplastics: recent progress and research trends, *Sci. Total Environ.* 757 (2021), 143875, <https://doi.org/10.1016/j.scitotenv.2020.143875>.
- [64] T. Saito, A. Isogai, Ion-exchange behavior of carboxylate groups in fibrous cellulose oxidized by the TEMPO-mediated system, *Carbohydr. Polym.* 61 (2005) 183–190, <https://doi.org/10.1016/j.carbpol.2005.04.009>.
- [65] N. Fiol, M.G. Vázquez, M. Pereira, Q. Tarrés, P. Mutjé, M. Delgado-Aguilar, TEMPO-oxidized cellulose nanofibers as potential Cu(II) adsorbent for wastewater treatment, *Cellulose* 26 (2019) 903–916, <https://doi.org/10.1007/s10570-018-2106-7>.
- [66] Z. Karim, M. Hakalahti, T. Tammelin, A.P. Mathew, In situ TEMPO surface functionalization of nanocellulose membranes for enhanced adsorption of metal ions from aqueous medium, *RSC Adv.* 7 (2017) 5232–5241, <https://doi.org/10.1039/C6RA25707K>.
- [67] R. Si, C. Wu, D. Yu, Q. Ding, R. Li, Novel TEMPO-oxidized cellulose nanofiber/polyvinyl alcohol/polyethyleneimine nanoparticles for Cu²⁺ removal in water, *Cellulose* 28 (2021) 10999–11011, <https://doi.org/10.1007/s10570-021-04236-4>.
- [68] V.W.D. Chui, K.W. Mok, C.Y. Ng, B.P. Luong, K.K. Ma, Removal and recovery of copper(II), chromium(III), and nickel(II) from solutions using crude shrimp chitin packed in small columns, *Environ. Int.* 22 (1996) 463–468, [https://doi.org/10.1016/0160-4120\(96\)00034-7](https://doi.org/10.1016/0160-4120(96)00034-7).
- [69] J. Lerivrey, B. Dubois, P. Decock, G. Micera, J. Urbanska, H. Kozłowski, Formation of D-glucosamine complexes with Cu(II), Ni(II) and Co(II) ions, *Inorg. Chim. Acta* 125 (1986) 187–190, [https://doi.org/10.1016/S0020-1693\(00\)81209-8](https://doi.org/10.1016/S0020-1693(00)81209-8).
- [70] C. Pakula, R. Stamminger, Electricity and water consumption for laundry washing by washing machine worldwide, *Energ. Eff.* 3 (2010) 365–382, <https://doi.org/10.1007/s12053-009-9072-8>.
- [71] A. Herrera, M. Asensio, I. Martínez, A. Santana, T. Packard, M. Gómez, Microplastic and tar pollution on three Canary Islands beaches: an annual study, *Mar. Pollut. Bull.* 129 (2018) 494–502, <https://doi.org/10.1016/j.marpolbul.2017.10.020>.
- [72] J.D. Redlinger-Pohn, M. Liverts, F. Lundell, Parameter regimes and rates of fibre collection on screens of various design, *Sep. Purif. Technol.* 259 (2021), 118053, <https://doi.org/10.1016/j.seppur.2020.118053>.